Alumina Polymorphism in the Circumstellar Dust Shells of Asymptotic Giant Branch Stars

Benjamin A. Sargent[1,2]

[1] Space Telescope Science Institute, 3700 San Martin Drive, Baltimore, MD 21218, USA; sargent@stsci.edu
[2] Center for Imaging Science and Laboratory for Multiwavelength Astrophysics, Rochester Institute of Technology, 54 Lomb Memorial Drive, Rochester NY 14623, USA

Abstract

Many emission features remain unidentified in the infrared spectra of asymptotic giant branch (AGB) stars. In particular, features at ~11, 20, 28, and 32 μm have been noted in mid-infrared spectra of oxygen-rich AGB stars. Here, I present models of dust excess emission in 36 spectra of 24 AGB stars from the Short Wavelength Spectrometer on board the *Infrared Space Observatory* and the Infrared Spectrograph on the *Spitzer Space Telescope*. The models include opacities of grains composed of mixtures of various polymorphs of alumina obtained by preparing bayerite and boehmite at high temperatures, and these dust components provide satisfactory fits to the 11, 20, 28, and 32 μm features. Though not a direct conclusion from this study, the presence of grains of the various polymorphs of aluminas in circumstellar dust shells around AGB stars suggests that corundum may have a role in giving rise to the 13 μm feature.

Key words: circumstellar matter – infrared: stars

Supporting material: machine-readable table

1. Introduction

An asymptotic giant branch (AGB) star is a star that has reached the penultimate stage of its life, when it expels its own material in a massive outflow, losing a large fraction of its mass in the process. It is thought that dust forms in the outflow, and then it is pushed away from the star by the star's radiation pressure (e.g., see Höfner et al. 2016). The dust then collectively pushes gas outward with it, driving the outflow.

AGB stars can be classified according to their photospheric abundance ratios, which are typically reflected in the composition of their circumstellar dust. AGB stars with a C/O ratio greater than unity are carbon-rich (C-rich) AGB stars (or "carbon stars"), and they tend to have circumstellar shells with dust that readily forms in such an environment—silicon carbide (SiC; Treffers & Cohen 1974), magnesium sulfide (MgS; Nuth et al. 1985), and carbonaceous material that is thought to be amorphous carbon (Rowan-Robinson & Harris 1983; Martin & Rogers 1987) but could alternatively be graphite (see the discussion by Speck et al. 2009). See also Messenger et al. (2013) for a discussion of MgS around C-rich AGB stars, and see also Thompson et al. (2006) for a discussion of SiC around C-rich AGB stars. AGB stars with a C/O ratio less than unity are oxygen-rich (O-rich) AGB stars, and they tend to have circumstellar dust composed of silicates, oxides, and other oxygen-rich compounds. S-type AGB stars are another type of AGB star. Smolders et al. (2012) performed a *Spitzer*-IRS survey of 87 S-type AGB stars in the Galaxy and find the circumstellar material to be an interesting mix of various compounds, though many of these stars' spectra suggested O-rich dust like silicates and alumina (Al_2O_3). This is not inconsistent with the findings of Smith & Lambert (1990), who find the C/O values for M, MS, and S stars to be well less than unity.

Both O-rich and S-type AGB stars show evidence for alumina dust. Laboratory studies by Begemann et al. (1997) produced infrared optical constants for two forms of amorphous alumina (compact and porous) that are widely used when modeling these stars. The emission from this amorphous

alumina could be described as a very broad emission feature that peaks near 11–12 μm (in between the 10 and 20 μm amorphous silicate features) and tapers off gradually to longer wavelengths. In addition, many stars that show this broad feature also have a sharp emission feature at ~13 μm (Sloan et al. 2003a). This feature was seen in spectra of M stars from missions as far back as the *Infrared Astronomical Satellite* (*IRAS*; e.g., Little-Marenin & Price 1986). The identification of this feature is controversial, but there are suggestions that the carrier is corundum (Glaccum 1999; DePew et al. 2006), which is the α polymorph of alumina. The 13 μm feature frequently appears along with spectral structure between about 9 and 11 μm (Sloan et al. 1996, 2003a; Speck et al. 2000).

Polymorphs are crystals that are compositionally the same but have different crystalline structures. Pitman et al. (2008) discussed the α and β polymorphs of SiC. Sargent et al. (2009) performed modeling of emission from dust grains in protoplanetary disks around T Tauri stars (TTSs), investigating various polymorphs of silica, SiO_2: α quartz, β quartz, tridymite, cristobalite, coesite, and stishovite. These studies note how the infrared spectra of polymorphs differ from each other and use these spectra to constrain the identity of the polymorph(s) present in the astronomical spectra; for example, Sargent et al. (2009) found the opacity of annealed silica from Fabian et al. (2000), composed of tridymite and cristobalite, to provide the best match to the TTS spectra. Alumina also has multiple polymorphs, including α-alumina and the so-called "transitional aluminas," including θ-, δ-, η-, and γ-alumina (Pecharromán et al. 1999), among others. As Pecharromán et al. (1999) noted, when the minerals bayerite, $Al(OH)_3$, which is a trihydrate, and boehmite, AlOOH, which is a monohydrate, are heated to sufficiently high temperatures, they transform into mixtures of various polymorphs of alumina, Al_2O_3 as determined from X-ray diffraction (XRD), infrared spectroscopy, and nuclear magnetic resonance (NMR) spectroscopy. These three techniques show that, as bayerite and boehmite are heated to progressively higher temperatures, the relative fraction of α-Al_2O_3

Table 1
Sample Information and Dust Model Parameters

Target (1)	d (kpc) (2)	A_V (3)	Spitzer Astronomical Observation Request (AOR) or ISO Astronomical Observation Template (AOT) (4)	Module Scalars (5)	Temp. (K) (6)	Amorphous Enstatite (7)	Corundum (8)	"Bayerite 1273 K" (9)	Amorphous Alumina (10)	"Boehmite 1173 K" (11)	$\frac{\chi^2}{\text{d.o.f.}}$ (12)
CE Lac[a]	2.2	0.57	18939648	1.039/ 1.000/	401	(33.1 ± 5.05) E–21	(0.00 ± 6.75) E–22	(2.66 ± 1.14) E–21	(0.00 ± 2.30) E–21	(0.00 ± 1.53) E–21	2.6595
...	...	...	Spitzer-IRS	none/none	249	(2.35 ± 262) E–20	(4.15 ± 3.92) E–21	(0.00 ± 3.78) E–21	(15.7 ± 1.10) E–20	(54.7 ± 5.84) E–21	...
CO Pyx[a]	1.6	0.29	18928896	1.070/ 1.000/	1400	(25.6 ± 7.21) E–22	(0.00 ± 1.55) E–22	(0.00 ± 1.58) E–22	(25.0 ± 3.89) E–22	(0.00 ± 2.29) E–22	3.7290
...	...	...	Spitzer-IRS	none/none	187	(0.00 ± 7.17) E–20	(1.12 ± 4.28) E–20	(10.1 ± 7.09) E–21	(46.4 ± 3.71) E–20	(10.1 ± 1.49) E–20	...
CSS 472[a]	4.0	0.93	18927360	1.096/ 1.000/	553	(7.00 ± 3.47) E–21	(0.00 ± 7.85) E–22	(12.8 ± 6.39) E–22	(0.00 ± 1.58) E–21	(9.36 ± 9.06) E–22	1.1821
...	...	...	Spitzer-IRS	none/none	219	(0.00 ± 4.18) E–20	(3.84 ± 18.1) E–20	(0.00 ± 5.22) E–21	(13.9 ± 1.96) E–20	(56.3 ± 9.03) E–21	...
CSS 480[a]	1.8	0.78	18927872	1.080/ 1.000/	1400	(16.7 ± 5.53) E–22	(0.00 ± 1.07) E–22	(9.52 ± 2.03) E–22	(4.57 ± 3.55) E–22	(0.00 ± 2.60) E–22	5.1867
...	...	...	Spitzer-IRS	none/none	252	(2.47 ± 3.92) E–20	(19.4 ± 7.39) E–21	(0.00 ± 4.13) E–21	(11.3 ± 1.69) E–20	(91.8 ± 8.29) E–21	...
CSS 1336[a]	1.8	0.68	18940416	1.038/ 1.000/	1138	(3.53 ± 3.00) E–22	(0.00 ± 4.85) E–23	(0.00 ± 1.18) E–22	(0.00 ± 1.68) E–22	(2.12 ± 14.0) E–23	0.82865
...	...	...	Spitzer-IRS	none/none	283	(0.00 ± 1.13) E–20	(8.37 ± 14.6) E–22	(1.31 ± 1.94) E–21	(15.4 ± 4.44) E–21	(5.10 ± 2.79) E–21	...
DL Cha[b]	0.44	0.73	5642240	none/ none/	310	(143 ± 3.66) E–19	(33.3 ± 7.29) E–20	(0.00 ± 9.76) E–20	(70.8 ± 2.10) E–19	(28.1 ± 1.42) E–19	65.769
...	...	...	Spitzer-IRS	1.157/ 0.684	105	(34.6 ± 5.02) E–17	(0.00 ± 5.71) E–17	(0.00 ± 2.59) E–18	(0.00 ± 2.11) E–17	(193 ± 7.69) E–18	...
EP Aqr[b]	0.12	0.058	38600922	n/a	295	(368 ± 7.38) E–18	(5.49 ± 1.09) E–18	(6.89 ± 1.44) E–18	(71.3 ± 3.35) E–18	(65.6 ± 2.23) E–18	33.239
...	...	...	ISO-SWS	...	75	(0.00 ± 3.73) E–15	(3.08 ± 18.4) E–15	(0.00 ± 2.13) E–16	(23.0 ± 1.65) E–15	(21.3 ± 5.46) E–16	...
EP Aqr[b]	0.12	0.058	53501243	n/a	280	(409 ± 8.23) E–18	(5.77 ± 1.24) E–18	(0.00 ± 1.27) E–18	(93.8 ± 3.72) E–18	(72.9 ± 2.31) E–18	50.437
...	...	...	ISO-SWS	...	70	(0.00 ± 4.57) E–15	(1.42 ± 3.29) E–14	(0.00 ± 1.86) E–16	(23.2 ± 2.00) E–15	(0.00 ± 6.28) E–16	...
FI Lyr[b]	0.45	0.33	82700735	n/a	338	(158 ± 4.06) E–19	(26.9 ± 9.25) E–20	(1.70 ± 1.47) E–19	(63.9 ± 2.77) E–19	(76.4 ± 1.91) E–19	105.73
...	...	...	ISO-SWS	...	59	(0.00 ± 4.45) E–15	(1.58 ± 2.24) E–14	(7.23 ± 2.65) E–16	(20.3 ± 1.93) E–15	(7.47 ± 6.50) E–16	...
GH Aur[a]	1.0	0.44	18920192	1.097/ 1.000/	1400	(10.6 ± 8.24) E–22	(0.00 ± 1.47) E–22	(4.65 ± 2.89) E–22	(56.0 ± 5.27) E–22	(0.00 ± 3.76) E–22	2.4922
...	...	...	Spitzer-IRS	none/none	159	(8.10 ± 2.86) E–19	(2.54 ± 12.2) E–20	(0.00 ± 2.69) E–20	(8.29 ± 1.36) E–19	(39.4 ± 5.45) E–20	...
g Her[b]	0.12	0.012	11103947	n/a	340	(32.4 ± 1.10) E–18	(25.4 ± 3.83) E–19	(44.1 ± 3.77) E–19	(314 ± 8.88) E–19	(141 ± 5.49) E–19	53.800
...	...	...	ISO-SWS	...	60						...

Table 1
(Continued)

Target (1)	d (kpc) (2)	A_V (3)	Spitzer Astronomical Observation Request (AOR) or ISO Astronomical Observation Template (AOT) (4)	Module Scalars (5)	Temp. (K) (6)	Amorphous Enstatite (7)	Corundum (8)	"Bayerite 1273 K" (9)	Amorphous Alumina (10)	"Boehmite 1173 K" (11)	$\frac{\chi^2}{\text{d.o.f.}}$ (12)
						(0.00 ± 4.74) E−15	(0.00 ± 5.12) E−14	(9.22 ± 37.7) E−17	(0.00 ± 2.26) E−15	(167 ± 9.52) E−16	
g Her[b]	0.12	0.012	42401416	n/a	644	(0.00 ± 1.06) E−19	(45.0 ± 6.73) E−20	(0.00 ± 4.22) E−20	(57.0 ± 1.58) E−19	(0.00 ± 8.98) E−20	141.88
...	...	...	ISO-SWS	...	274	(46.8 ± 2.45) E−18	(0.00 ± 7.91) E−19	(73.0 ± 5.27) E−19	(0.00 ± 1.44) E−18	(286 ± 8.40) E−19	...
g Her[b]	0.12	0.012	80000104	n/a	430	(0.00 ± 1.05) E−20	(79.5 ± 9.83) E−20	(0.00 ± 1.18) E−19	(0.00 ± 2.14) E−19	(122 ± 1.53) E−19	1703.9
...	...	...	ISO-SWS	...	56	(0.00 ± 5.26) E−15	(11.2 ± 5.81) E−14	(51.9 ± 3.70) E−15	(0.00 ± 2.30) E−15	(92.0 ± 9.08) E−16	...
Leid 33062[c]	5.0[d]	0.37[d]	27856128	1.001/ 1.000/	1400	(25.9 ± 1.56) E−22	(0.00 ± 3.03) E−23	(8.24 ± 5.81) E−23	(114 ± 9.53) E−23	(0.00 ± 7.35) E−23	3.2027
...	...	...	Spitzer-IRS	none/none	188	(34.1 ± 3.03) E−20	(6.55 ± 8.98) E−21	(0.00 ± 2.96) E−21	(6.88 ± 1.33) E−20	(64.8 ± 6.05) E−21	...
NGC 104[e]	4.6[f]	0.12[f]	10866945	1.352/ 1.394/	623	(0.00 ± 1.62) E−22	(0.00 ± 1.15) E−22	(11.1 ± 2.21) E−22	(0.00 ± 3.53) E−22	(0.00 ± 2.78) E−22	27.752
SAW v13	...	...	Spitzer-IRS	none/1.000	195	(0.00 ± 1.76) E−20	(6.70 ± 6.77) E−21	(0.00 ± 3.74) E−21	(6.69 ± 1.41) E−20	(0.00 ± 6.15) E−21	...
NGC 104[e]	4.6[f]	0.12[f]	10867969	1.464/ 1.616/	320	(0.00 ± 2.08) E−21	(11.5 ± 8.15) E−22	(3.39 ± 1.61) E−21	(0.00 ± 2.99) E−21	(0.00 ± 2.19) E−21	12.239
SAW v21	...	...	Spitzer-IRS	none/1.000	136	(0.00 ± 1.80) E−19	(0.00 ± 8.24) E−20	(0.00 ± 2.80) E−20	(3.83 ± 1.15) E−19	(0.00 ± 4.60) E−20	...
NGC 104[e]	4.6[f]	0.12[f]	12979969	1.656/ 1.625/	365	(23.6 ± 7.14) E−21	(3.94 ± 8.97) E−22	(5.44 ± 2.14) E−21	(32.5 ± 3.53) E−21	(0.00 ± 2.80) E−21	7.2445
v4	...	...	Spitzer-IRS	none/1.000	111	(6.06 ± 1.29) E−18	(1.26 ± 8.20) E−19	(0.00 ± 1.56) E−19	(0.00 ± 6.99) E−19	(0.00 ± 2.91) E−19	...
NGC 104[e]	4.6[f]	0.12[f]	12979969	2.006/ 1.775/	1343	(0.00 ± 3.58) E−22	(0.00 ± 6.74) E−23	(5.09 ± 1.92) E−22	(18.7 ± 2.60) E−22	(0.00 ± 2.18) E−22	12.087
v8	...	...	Spitzer-IRS	none/1.000	168	(16.1 ± 1.68) E−19	(3.81 ± 3.79) E−20	(0.00 ± 2.20) E−20	(0.00 ± 7.69) E−20	(0.00 ± 3.59) E−20	...
NGC 5927[g]	7.8[h]	1.4[h]	21741568	1.040/ 1.000/	482	(145 ± 9.45) E−22	(3.26 ± 1.43) E−22	(3.62 ± 4.16) E−22	(41.1 ± 5.29) E−22	(12.2 ± 4.67) E−22	1.8741
v1	...	...	Spitzer-IRS	none/none	199	(1.24 ± 3.78) E−20	(0.00 ± 4.18) E−21	(1.75 ± 5.80) E−21	(8.33 ± 1.39) E−20	(37.1 ± 8.59) E−21	...
NGC 6352[g]	5.9[i]	0.65[i]	21742848	1.081/ 1.000/	1184	(29.9 ± 4.05) E−22	(0.00 ± 6.96) E−23	(4.04 ± 1.46) E−22	(20.7 ± 2.25) E−22	(0.00 ± 1.72) E−22	1.6623
v5	...	...	Spitzer-IRS	none/none	199	(30.8 ± 4.88) E−20	(1.49 ± 1.16) E−20	(0.00 ± 5.74) E−21	(13.7 ± 2.04) E−20	(5.59 ± 1.01) E−20	...
S Pav[b]	0.19	0.071	14401702	n/a	310	(110 ± 3.07) E−18	(33.8 ± 9.04) E−19	(53.6 ± 9.72) E−19	(103 ± 2.34) E−18	(26.8 ± 1.42) E−18	52.050
...	...	...	ISO-SWS	...	60	(0.00 ± 1.05) E−14	(0.00 ± 9.48) E−14	(59.1 ± 8.49) E−16	(0.00 ± 4.81) E−15	(37.7 ± 2.11) E−15	...
J18284939[j]	0.88	1.6	13210624		1400						12.788

3

Table 1
(Continued)

Target (1)	d (kpc) (2)	A_V (3)	Spitzer Astronomical Observation Request (AOR) or ISO Astronomical Observation Template (AOT) (4)	Module Scalars (5)	Temp. (K) (6)	Amorphous Enstatite (7)	Corundum (8)	"Bayerite 1273 K" (9)	Amorphous Alumina (10)	"Boehmite 1173 K" (11)	$\frac{\chi^2}{\text{d.o.f.}}$ (12)
				1.086/ 1.000/		(2.07 ± 9.55) E–22	(1.58 ± 2.88) E–22	(8.20 ± 4.53) E–22	(116 ± 7.71) E–22	(3.70 ± 5.85) E–22	
+000604	⋯	⋯	Spitzer-IRS	none/none	187	(25.7 ± 2.40) E–19	(15.8 ± 8.57) E–20	(1.95 ± 2.36) E–20	(0.00 ± 1.06) E–19	(118 ± 4.67) E–20	⋯
ST Her[b]	0.27	0.051	41901305	n/a	420	(96.3 ± 2.84) E–19	(3.28 ± 1.18) E–19	(0.00 ± 1.34) E–19	(50.7 ± 3.52) E–19	(137 ± 2.54) E–19	123.60
⋯	⋯	⋯	ISO-SWS	⋯	75	(35.0 ± 1.35) E–15	(5.16 ± 4.69) E–15	(48.2 ± 7.53) E–17	(0.00 ± 5.50) E–16	(0.00 ± 1.77) E–16	⋯
T Cep[b]	0.18	0.34	26300141	n/a	410	(62.3 ± 6.60) E–19	(3.26 ± 3.24) E–19	(7.60 ± 3.25) E–19	(162 ± 7.94) E–19	(298 ± 5.21) E–19	69.445
⋯	⋯	⋯	ISO-SWS	⋯	131	(109 ± 9.34) E–17	(47.1 ± 9.62) E–17	(0.00 ± 5.96) E–18	(0.00 ± 4.05) E–17	(6.21 ± 1.46) E–17	⋯
T Cep[b]	0.18	0.34	34601646	n/a	1400	(237 ± 7.11) E–20	(0.00 ± 4.02) E–20	(0.00 ± 6.14) E–20	(18.9 ± 1.12) E–19	(178 ± 8.85) E–20	77.843
⋯	⋯	⋯	ISO-SWS	⋯	190	(0.00 ± 2.01) E–17	(5.85 ± 1.16) E–17	(42.6 ± 3.35) E–18	(54.6 ± 1.58) E–17	(94.8 ± 6.73) E–18	⋯
T Cep[b]	0.18	0.34	40800106	n/a	1400	(223 ± 6.77) E–20	(0.00 ± 3.63) E–20	(0.00 ± 4.39) E–20	(21.3 ± 1.02) E–19	(206 ± 7.74) E–20	70.474
⋯	⋯	⋯	ISO-SWS	⋯	183	(0.00 ± 1.80) E–17	(6.08 ± 1.29) E–17	(37.1 ± 2.89) E–18	(35.8 ± 1.44) E–17	(80.2 ± 5.91) E–18	⋯
T Cep[b]	0.18	0.34	42602251	n/a	1400	(223 ± 6.89) E–20	(0.00 ± 3.53) E–20	(0.00 ± 5.36) E–20	(23.5 ± 1.08) E–19	(201 ± 8.32) E–20	84.160
⋯	⋯	⋯	ISO-SWS	⋯	175	(0.00 ± 2.67) E–17	(8.93 ± 1.79) E–17	(56.0 ± 3.84) E–18	(54.5 ± 1.91) E–17	(87.7 ± 7.83) E–18	⋯
T Cep[b]	0.18	0.34	51401256	n/a	1400	(297 ± 8.83) E–20	(0.00 ± 3.89) E–20	(0.00 ± 5.50) E–20	(18.4 ± 1.36) E–19	(34.5 ± 1.08) E–19	88.218
⋯	⋯	⋯	ISO-SWS	⋯	160	(0.00 ± 8.25) E–17	(19.7 ± 3.92) E–17	(97.1 ± 7.36) E–18	(139 ± 3.85) E–17	(8.44 ± 1.54) E–17	⋯
T Cep[b]	0.18	0.34	57501031	n/a	335	(98.4 ± 2.88) E–18	(37.7 ± 9.85) E–19	(86.4 ± 9.19) E–19	(110 ± 2.46) E–18	(28.9 ± 1.44) E–18	57.110
⋯	⋯	⋯	ISO-SWS	⋯	60	(0.00 ± 1.32) E–14	(6.23 ± 13.8) E–14	(0.00 ± 7.96) E–16	(0.00 ± 5.49) E–15	(33.8 ± 2.01) E–15	⋯
T Cep[b]	0.18	0.34	66101436	n/a	330	(63.9 ± 2.10) E–18	(31.7 ± 7.56) E–19	(19.6 ± 5.59) E–19	(79.0 ± 1.79) E–18	(303 ± 9.94) E–19	37.150
⋯	⋯	⋯	ISO-SWS	⋯	75	(0.00 ± 1.43) E–15	(9.23 ± 10.2) E–15	(0.00 ± 8.30) E–17	(0.00 ± 6.27) E–16	(19.4 ± 2.36) E–16	⋯
T Cep[b]	0.18	0.34	74602101	n/a	360	(51.3 ± 1.63) E–18	(19.0 ± 5.85) E–19	(48.7 ± 5.26) E–19	(73.2 ± 1.44) E–18	(122 ± 8.37) E–19	39.335
⋯	⋯	⋯	ISO-SWS	⋯	75	(0.00 ± 1.55) E–15	(5.86 ± 9.92) E–15	(6.95 ± 11.5) E–17	(0.00 ± 7.11) E–16	(49.2 ± 2.86) E–16	⋯
T Cet[b]	4.6	0.066	37801819	n/a	1400	(0.00 ± 1.26) E–21	(11.5 ± 4.20) E–21	(0.00 ± 8.11) E–21	(0.00 ± 1.18) E–20	(40.4 ± 1.08) E–20	133.76
⋯	⋯	⋯	ISO-SWS	⋯	183	(0.00 ± 2.47) E–18	(2.82 ± 1.48) E–18	(153 ± 9.04) E–19	(65.1 ± 2.54) E–18	(0.00 ± 1.32) E–18	⋯

Table 1
(Continued)

Target (1)	d (kpc) (2)	A_V (3)	Spitzer Astronomical Observation Request (AOR) or ISO Astronomical Observation Template (AOT) (4)	Module Scalars (5)	Temp. (K) (6)	Amorphous Enstatite (7)	Corundum (8)	"Bayerite 1273 K" (9)	Amorphous Alumina (10)	"Boehmite 1173 K" (11)	$\frac{\chi^2}{\text{d.o.f.}}$ (12)
T Cet[b]	4.6	0.066	55502308	n/a	1400	(115 ± 9.01) E−21	(0.00 ± 8.05) E−21	(0.00 ± 1.19) E−20	(50.2 ± 2.12) E−20	(13.8 ± 1.86) E−20	69.935
...	...	...	ISO-SWS	...	185	(105 ± 9.91) E−18	(15.3 ± 2.90) E−18	(13.7 ± 1.75) E−18	(143 ± 5.20) E−18	(49.7 ± 2.66) E−18	...
T Mic[b]	0.19	0.091	14401129	n/a	345	(35.0 ± 1.18) E−18	(16.6 ± 4.53) E−19	(22.0 ± 5.27) E−19	(45.7 ± 1.16) E−18	(213 ± 7.30) E−19	58.286
...	...	...	ISO-SWS	...	58	(0.00 ± 8.82) E−15	(0.00 ± 7.77) E−14	(117 ± 8.37) E−16	(0.00 ± 4.21) E−15	(27.9 ± 2.04) E−15	...
T Mic[b]	0.19	0.091	87201305	n/a	310	(48.7 ± 1.54) E−18	(18.7 ± 4.90) E−19	(22.5 ± 5.03) E−19	(49.6 ± 1.26) E−18	(216 ± 7.66) E−19	59.024
...	...	...	ISO-SWS	...	64	(0.00 ± 3.45) E−15	(9.99 ± 29.3) E−15	(4.85 ± 2.51) E−16	(0.00 ± 1.61) E−15	(120 ± 6.30) E−16	...
Y UMa[b]	0.31	0.039	60200502	n/a	410	(108 ± 3.18) E−19	(1.80 ± 1.13) E−19	(0.00 ± 1.31) E−19	(87.6 ± 3.03) E−19	(48.2 ± 2.10) E−19	66.282
...	...	...	ISO-SWS	...	187	(12.3 ± 9.77) E−18	(11.0 ± 2.98) E−18	(3.36 ± 1.11) E−18	(0.00 ± 4.53) E−18	(55.3 ± 2.09) E−18	...

Notes. Column (1): Target name. (2): Distance to object in kilo-parsecs obtained (unless otherwise indicated) from parallaxes reported by GAIA data release 2 (DR2; Gaia Collaboration et al. 2016; Arenou et al. 2018; Gaia Collaboration et al. 2018; Luri et al. 2018). Column (3): Extinction at V band, A_V, determined (unless otherwise indicated) from Drimmel et al. (2003), assuming the distance given in Column 2. Column (4): the AOR number, if Spitzer-IRS data or the AOT number, if ISO-SWS data. Column (5): Scalars applied to raw reduced Spitzer-IRS spectra from individual modules, with the entries in the following order: Short-Low/Long-Low/Short-High/Long-High (DL Cha is a special case, where the Spitzer-IRS spectrum was appended to the ISO-SWS spectrum (AOT 62804032) at the shortest wavelength of its Spitzer-IRS Short-High spectrum). Column (6): One of two dust model temperatures (Kelvin). Columns (7)–(11): mass weights, in units of grams per square centimeter, equal to mass divided by the square of Earth-target distance and its uncertainty for all dust species at the temperature specified in Column (6). One dust model is completely specified by two adjacent rows—the row following the object's name and the row beneath that one. Column (12): χ^2 per degree of freedom, determined over $8.0 < \lambda < 37 \, \mu m$. The column names of "Bayerite 1273 K" and "Boehmite 1173 K" for columns 9 and 11, respectively, are included in quotes because the samples no longer contain bayerite or boehmite, respectively, as noted in Section 3 of the text, but were obtained by heating these minerals at these temperatures.
[a] Sources from Smolders et al. (2012).
[b] Sources from Sloan et al. (2003a).
[c] Source from McDonald et al. (2011a).
[d] Leid 33062 belongs to ω Cen. For this cluster, I assume the same as McDonald et al. (2011a); namely, the distance is 5 kpc, and $E(B - V) = 0.12$. $A_V = 3.1^* R_V$ is assumed (Mathis 1990).
[e] Sources from Lebzelter et al. (2006).
[f] For NGC 104 (47 Tuc), I assume the same as McDonald et al. (2011b); namely, the distance is 4.6 kpc, and $E(B - V) = 0.04$. $A_V = 3.1^* R_V$ is assumed (Mathis 1990).
[g] Sources from Sloan et al. (2010).
[h] For NGC 5927, I assume 7.8 kpc and $E(B - V) = 0.46$ (Sloan et al. 2010) and $A_V = 3.1^* E(B - V)$ (Mathis 1990).
[i] For NGC 6352, I assume 5.9 kpc and $E(B - V) = 0.21$ (Sloan et al. 2010) and $A_V = 3.1^* E(B - V)$ (Mathis 1990).
[j] Source from Olofsson et al. (2009).

(This table is available in machine-readable form.)

increases at the expense of the other polymorphs (Pecharromán et al. 1999).

Sloan et al. (2003a) noted that many stars that show emission from the 13 μm feature also show emission features at other wavelengths—20 and 28 μm—whose strengths appear to be correlated with that of the 13 μm feature. They also note a 32 μm emission feature, though their study did not find correlation with the 13 μm feature. In addition, they note the presence of another feature near 11 μm. In this study, I suggest that the 11, 20, 28, and 32 μm features are due to polymorphs of alumina.

2. Data

The spectra analyzed in this study come both from the *Spitzer Space Telescope* (Werner et al. 2004) Infrared Spectrograph (IRS; Houck et al. 2004) and from the *Infrared Space Observatory* (*ISO*; Kessler et al. 1996) Short Wavelength Spectrometer (SWS; Leech et al. 2003). My sample of spectra were chosen from among previous studies of AGB stars (see Table 1) for their relatively prominent 11, 20, 28, and 32 μm emission features. I present the sample in Table 1. The targets are distributed over the sky, though they all are Galactic AGB stars. The *ISO*-SWS spectra studied here are obtained from a website[3] made available to the public by Greg Sloan (see Sloan et al. 2003b).

The raw data for the *Spitzer*-IRS spectra studied here were downloaded from the *Spitzer* Heritage Archive.[4] These data were reduced using an automated pipeline, developed by Elise Furlan, that runs the SMART (Higdon et al. 2004) software developed to reduce *Spitzer*-IRS data. Bad pixels were fixed as described by Sargent et al. (2009). Low-resolution data were extracted by optimal point source extraction (Lebouteiller et al. 2010), while high-resolution data were extracted by full-slit extraction. The flux-calibrated spectra from the various orders and modules were then averaged, with the flux uncertainties determined from the standard deviation of the mean. The order and module spectra were then merged, and the ends of orders were trimmed. To account for differences in fluxes between modules, I scaled the modules to match each other's fluxes (e.g., Sargent et al. 2009).

Next, I corrected each *ISO*-SWS and *Spitzer*-IRS spectrum for extinction assuming the A_V provided in Table 1 using the Drimmel et al. (2003) extinction model, assuming distances from GAIA parallaxes (Table 1), and assuming the extinction curve for $0.3 < A_K < 1$ from McClure (2009). I then fit PHOENIX stellar-photosphere spectral models for solar metallicity ranging from $T_{\rm eff} = 2000–4700$ K and $\log(g)$ ranging from -0.5 to $+5.5$ (Kučinskas et al. 2005, 2006) to the 5.3–8 μm part of each spectrum, subtracted the best-fit photosphere model, and retained the flux uncertainties for the residual (i.e., stellar-photosphere-subtracted) spectra. This subtraction of the stellar-photosphere emission to analyze the dust excess emission was also performed by Guha Niyogi et al. (2011). I convolved the residual spectra from *Spitzer*-IRS Short-High and Long-High observations (DL Cha and the targets from NGC 104) and *ISO*-SWS observations to the resolution of Short-Low and Long-Low.

Justtanont et al. (1998) noted that the 13 μm feature strength is correlated with those of the CO_2 emission lines between

10 and 20 μm wavelength; however, this study focuses on modeling the emission from circumstellar dust. No attempt is made in this analysis to model the emission or absorption from CO_2 or any other gas. Leaving them in the spectra but not modeling them would affect attempts to model the dust emission. Therefore, wavelengths over the ranges 13.4–13.6, 13.8–14.0, 14.7–15.1, 15.3–15.5, and 16.1–16.3 μm were removed due to CO_2 line contamination.

3. Analysis

As Sloan et al. (2003a) noted, AGB stars with relatively stronger emission features at 13, 20, and 28 μm often have lower infrared excesses. I therefore take an optically thin modeling approach that is similar to the models of emission from dust in protoplanetary disks around TTSs presented by (Sargent et al. 2009). One critical difference is that such protoplanetary disks are quite optically thick at mid-infrared wavelengths, but the circumstellar shells around the AGB stars in my sample are likely not. The models in this study, therefore, do not include any blackbody component. They are of the form

$$F_\nu(\lambda)^{\rm mod} = B_\nu(\lambda, T_c)\left[\sum_j a_{c,j}\kappa_j(\lambda)\right]$$
$$+ B_\nu(\lambda, T_w)\left[\sum_j a_{w,j}\kappa_j(\lambda)\right]. \quad (1)$$

This equation includes two sums with terms of the form assumed in the dust modeling by Sargent et al. (2006); namely, the product of dust opacity times a Planck function times a constant. The product of opacity times Planck function times constant arises from the assumption that each of the dust grain populations at each of the two temperatures are optically thin over the wavelengths of concern (over *ISO*-SWS and *Spitzer*-IRS spectral wavelengths). The left-hand side of this equation is the total flux from the dust grains in the model, to be compared directly to the stellar-photosphere-subtracted flux residuals. On the right-hand side, $B_\nu(\lambda, T)$ is the Planck function evaluated at temperature T and wavelength λ, $\kappa_j(\lambda)$ is the opacity (total grain cross-section per mass) of dust species j evaluated at wavelength λ, and $a_{c,j}$ and $a_{w,j}$ are the mass weights (equal to mass in the dust species at one temperature divided by the square of the distance from Earth to the target; for more, see Sargent et al. 2009) of dust species j for the cool and warm dust population(s) of that species, respectively. Like the protoplanetary disk models, these models have dust at only two temperatures, as this is sufficient to model dust emission spanning the wavelength range covered by *Spitzer*-IRS spectra (5–37 μm). This is perhaps more desirable than a single-temperature dust modeling approach such as that taken by Guha Niyogi et al. (2011), though a more thorough approach to modeling the dust from these AGB stars might be to adopt a range of dust temperatures as done by Simpson (1991). However, such an approach relies on assumptions regarding the distribution of dust at various temperatures. The two-temperature optically thin approach has the "Occam's Razor" advantage of being simple.

The opacities used in the modeling were as follows. To match the 10 μm feature, amorphous silicates were included, using complex indices of refraction for amorphous enstatite MgSiO$_3$ from Day (1979), assuming a spheroid with depolarization parameters (L_1, L_2) of (0.25, 0.25; see
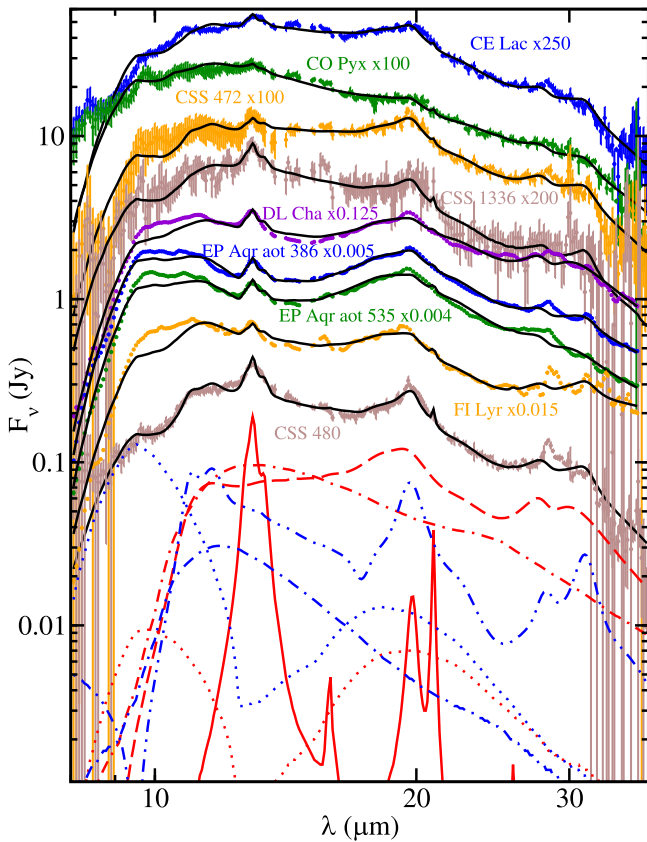

Figure 1. This plot shows spectra and their models, both of which have been scaled by the indicated amounts in this figure, for clarity. The residual spectra with error bars are either brown, orange, green, blue, or violet, and the best-fit model for each is a thick black line on top of the residuals. For *ISO* spectra, only the first three digits of the AOT number are given. The blue and red curves at the bottom are the components of the model fit to CSS 480 at the higher and lower temperatures, respectively, used in its model (see Table 1). The linestyles for the model components are: solid line, corundum; dotted line, amorphous silicate; dashed–dotted line, amorphous alumina; long-dashed line, sample obtained by heating boehmite at 1173 K; dashed–dotted–dotted line, sample obtained by heating bayerite at 1273 K.

Bohren & Huffman 1983) to compute its opacity. There are many options for optical constants sets of amorphous silicates but a detailed investigation of which one(s) best fit amorphous silicate emission from dust grains in the circumstellar shells of AGB stars is beyond the scope of this Letter and is the subject of a work in progress (B. A. Sargent et al. 2018, in preparation). For a discussion of the multiple amorphous silicate optical constants sets available, see Speck et al. (2011). It should be noted that the observed $10\,\mu m$ features in the present sample seem to require a narrow $10\,\mu m$ feature in the amorphous silicate opacity, and the one used, amorphous enstatite from Day (1979), has a $10\,\mu m$ feature FWHM among the lower ones studied by Speck et al. (2011).

To match the $13\,\mu m$ feature, corundum was included, using the complex dielectric function for the ordinary and extra-ordinary rays of corundum at 295K from Thomas et al. (1998), assuming a tCDE shape distribution (see Sargent et al. 2009) bound by the (L_1, L_2) vertices (0.31, 0.31), (0.31, 0.34), and (0.34, 0.31) to compute its opacity. As with quartz, corundum is an anisotropic material, with different optical properties for the ordinary ray and the extraordinary ray. Also as with quartz, the "$\frac{2}{3}\frac{1}{3}$ approximation" is used, following the discussion of

anisotropy by Fabian et al. (2001) and the implementation for a crystal with ordinary and extraordinary rays by Sargent et al. (2006, 2009). As with amorphous silicates, many different optical constants sets are available for corundum, but also as with amorphous silicates, a thorough investigation of which optical constant set(s) are the best is beyond the scope of this Letter. For a discussion of some available corundum optical constant sets, see Zeidler et al. (2013).

It was found that the complex dielectric function from Pecharromán et al. (1999) for the sample obtained by heating bayerite at 1273 K, assuming a spheroid with depolarization parameters of (0.35, 0.003), produced an opacity with 11, 20, 28, and $32\,\mu m$ features, so this component was included in the models. However, with only this component, the observed $20\,\mu m$ features in the residual spectra were found to be wider than those in the models. By adding the opacity of the sample obtained by heating boehmite at 1173 K, the width of the $20\,\mu m$ feature could be matched. This was done using the complex dielectric function for the sample obtained by heating boehmite at 1173 K from Pecharromán et al. (1999), assuming a spheroid with depolarization parameters of (0.35, 0.035). The complex dielectric functions of the samples obtained by heating bayerite and boehmite to various temperatures (Pecharromán et al. 1999) were derived by modeling the reflectance spectra of pellets obtained by pressing powders of these materials under great pressure. This method required Pecharromán et al. (1999) to assume an effective medium theory, such that a pellet is a mixture of one of their samples with a matrix of air. Pecharromán et al. (1999) noted that heating bayerite at $500°C$ eliminates the XRD pattern of bayerite, and they note that at $700°C$, the infrared reflectance spectrum of the boehmite sample no longer shows OH^- stretching bands. This must mean that the samples obtained from heating bayerite at 1273 K and from heating boehmite at 1173 K are no longer bayerite or boehmite, respectively. XRD performed by Pecharromán et al. (1999) of the sample of bayerite prepared at 1273 K suggests only θ-alumina was present, and their infrared and NMR spectroscopy confirms this. XRD of their sample obtained from heating boehmite to 1173 K (Pecharromán et al. 1999) suggests δ-alumina to be present, though some amounts of θ-alumina and α-alumina are present, as they deduce from XRD and infrared and NMR spectroscopy.

Even including the opacities of the samples obtained from bayerite heated at 1273 K and boehmite heated at 1173 K, the spectrum between the 10 and $20\,\mu m$ features still could not be matched sufficiently. Speck et al. (2000) found that a mixture of amorphous silicates and amorphous alumina could explain spectra showing broad mid-infrared features. Along these lines, the opacity of amorphous alumina was added, assuming the complex indices of refraction for amorphous alumina from Eriksson et al. (1981) using the table provided by Koike et al. (1995) and assuming a distribution of spheroid shapes similar to the continuous distribution of spheroids (Min et al. 2003), but computed discretely as the average of the set of opacities computed for spheroids of $(L_1 = N/24, L_2 = N/24)$, where N ranges from 0 to 12. For a discussion of various amorphous alumina optical constants sets, see Begemann et al. (1997). For this study, the various amorphous alumina optical constants sets mentioned by Begemann et al. (1997) were used in models of the present sample, and it was found that Eriksson et al. (1981) typically provided better fits than other amorphous
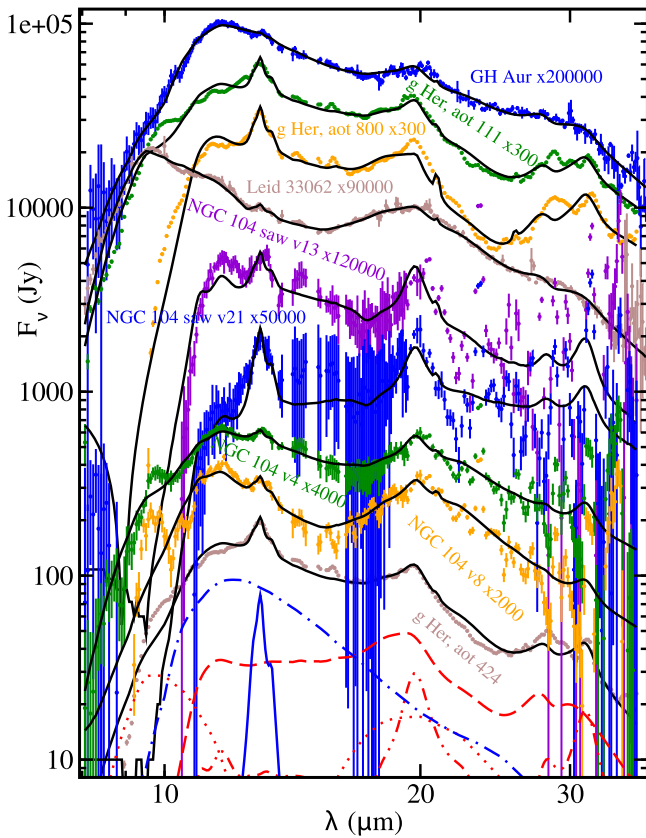
Figure 2. Same convention as for Figure 1, except that the model components at the bottom correspond to the best-fit model to g Her, AOT 42401416.
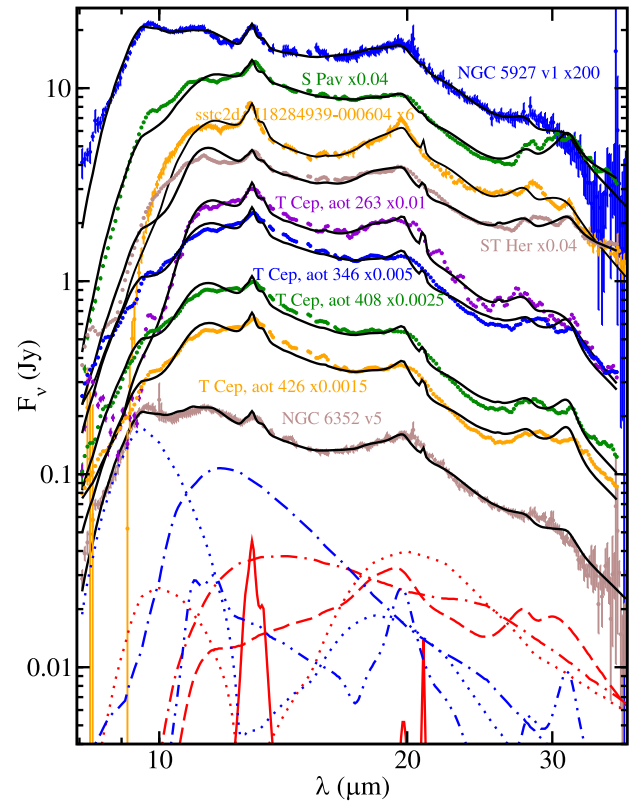

Figure 3. Same convention as for Figure 1, except that the model components at the bottom correspond to the best-fit model to NGC 6352 v5.

alumina optical constants sets, though this was not investigated rigorously as it was beyond the scope of this Letter.

The density for any given dust grain was assumed to be 3 grams per cm³. I used the χ-squared minimization method described by Sargent et al. (2009). For each residual spectrum, the model from Equation (1) returns the $a_{c,j}$ and $a_{w,j}$ mass weight parameters and the two temperatures, T_c and T_w, for the best-fit model. The best-fit model parameter values are given in Table 1. Uncertainties on the mass weights are determined as for Sargent et al. (2009).

4. Results

The spectral residuals and the best-fit models for each are presented in Figures 1–4. For each figure the model components for the bottom-most residual spectrum are indicated. The samples obtained by heating bayerite at 1273 K and boehmite at 1173 K are seen to provide good matches to the 20 μm features for most of the residual spectra. In addition, the 32 μm features are also often well matched in strength (if not always in central wavelength) by the models. The 28 μm features are matched somewhat well by these model components, though sometimes the model 28 μm feature is a bit too weak. The 11, 20, 28, and 32 μm features in these two opacities are very sensitive to the assumed ellipsoid depolarization parameters (i.e., shape). In order to produce these features, the grains of these components were assumed to be needle-like; i.e., much longer in one axis of the ellipsoid than in the others. In addition, the observed 11 μm feature is often well matched by the models (e.g., CSS 480 and CSS 1336 in Figure 1; NGC 104 v4 in Figure 2).
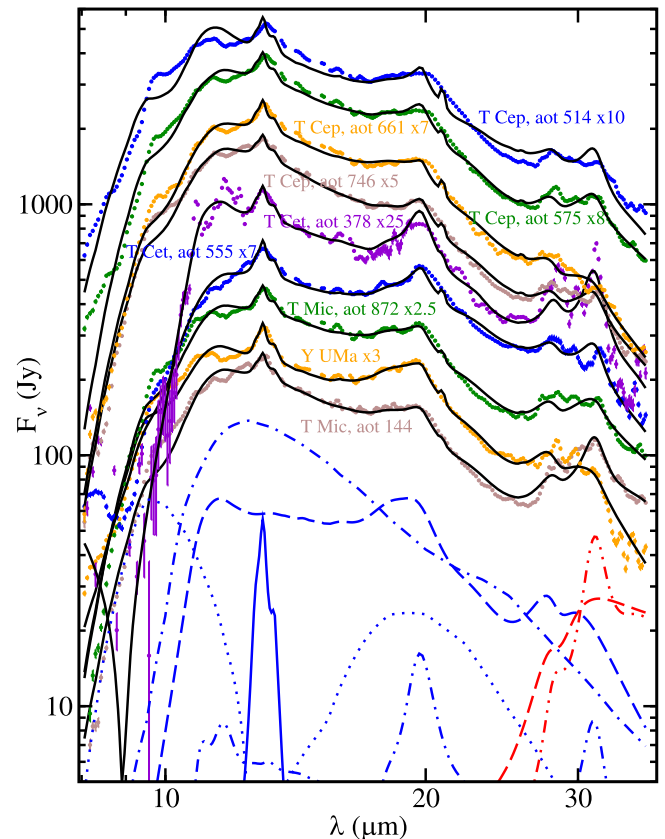

Figure 4. Same convention as for Figure 1, except that the model components at the bottom correspond to the best-fit model to T Mic, AOT 14401129.

The corundum fits the 13 μm features well and sometimes contributes to the 20 μm feature. It also produces a weak 21 μm feature that does not correspond to a feature in the data, though sometimes this feature is weak enough in a model that the model matches the spectrum well at 21 μm (e.g., for EP Aqr and CSS 472 in Figure 1; S Pav and NGC 5927 v1 in Figure 3; T Mic AOT 14401129 in Figure 4). DePew et al. (2006) showed that, for corundum, grain shape affects the appearance of spectral features for corundum. The shapes of corundum assumed for the models in my study are slightly oblate. This is consistent with the finding of Takigawa et al. (2015) that corundum condensed in circumstellar environments should be slightly oblate. The 21 μm feature from the corundum component to the model of CSS 480 in Figure 1 is not present in the model spectrum of corundum shown by DePew et al. (2006), and the 20 μm feature from corundum that can be seen in the CSS 480 model in Figure 1 is not present in the model spectrum of corundum shown by Guha Niyogi et al. (2011), but the grain shapes and optical constants assumed here are not the same as those assumed by DePew et al. (2006) or Guha Niyogi et al. (2011). It is not the intention of this Letter to claim corundum as the carrier of the 13 μm feature. It is included in my models because none of the other model components or the opacities computed from the other Pecharromán et al. (1999) optical constants sets can fit the 13 μm feature satisfactorily, and other proposed carriers for the 13-micron feature tend to produce other features at undesirable wavelengths; e.g., spinel produces a 17 μm feature in addition to 13 and 32 μm features, and Sloan et al. (2003a) showed that the 16.8 μm feature seen in AGB spectra, proposed to arise from spinel, is too narrow to arise from dust.

As can be seen from the plots, the 10 μm feature is fit by the amorphous silicate with varying degrees of success. The opacities used in the modeling were judged to be the minimal number of opacities required to match the overall structure in the spectral residuals. It should be noted that alumina of various forms was used: corundum, the various polymorphs that Pecharromán et al. (1999) determined to be present in the samples of bayerite prepared at 1273 K and boehmite prepared at 1173 K (δ-alumina, θ-alumina, and α-alumina), and amorphous alumina. It may be that a wider "continuum" of polymorphs (and varying degrees of amorphousness) of alumina may be present in AGB dust shells than assumed here, but it is desired to keep the models as simple as possible.

5. Discussion and Conclusions

Tamanai et al. (2009) obtained extinction spectra for grains of varying compositions and shapes, and they conclude that the 13, 20, and 28 μm features arise primarily from TiO_2 (Anatase) and also, to a lesser degree, from spinel ($MgAl_2O_4$) and Al_2TiO_5. They present extinction curves for various samples of anatase grains, which have varying shape distributions. Some of the extinction curves have some of the features at 13, 20, and 28 μm, but none of the opacities that they present have sufficiently narrow features at all of these wavelengths; in addition, none of the anatase extinction curves that they present show narrow features at 11 and 32 microns, as I find with the sample obtained by heating bayerite at 1273 K. One of their spinel extinction curves shows a narrow 13 μm feature, and also a 32 μm feature similar to what can be seen in many of the spectra in my sample, but it also shows a moderately weaker feature of width similar to the 13 μm feature around

17–18 μm. Posch et al. (1999) noted the presence of a 16.8 μm feature and suggested that it arises from spinel. However, Sloan et al. (2003a) found this feature to be too narrow to be a dust feature. Finally, the Al_2TiO_5 curve, while it shows 13 and 28 μm features, also has a broad feature spanning 15–17 μm of strength similar to its 13 μm feature. For most of the spectra shown in Figures 1–4, this does not readily correspond to known features seen in AGB star spectra, with perhaps the exception of FI Lyr (Figure 1), but corundum also has a feature at this wavelength (see Figure 1). Tamanai et al. (2009) did include a sample of alumina (besides the α and γ polymorphs) containing a number of different polymorphs (χ, δ, and κ) whose extinction curve contains many peaks between 10 and 50 μm that do not match features seen in AGB spectra. However, the opacities of the samples obtained from heating bayerite at 1273 K and boehmite at 1173 K that I use in my models to provide 11, 20, 28, and 32 μm features contain θ-Al_2O_3, δ-Al_2O_3, and α-Al_2O_3, as Pecharromán et al. (1999) determined, and θ-Al_2O_3 was not studied by Tamanai et al. (2009).

Takigawa et al. (2014) presented a study of presolar alumina grains from the meteorites Semarkona, Bishunpur, and RC075, and they also conduct dissolution experiments on corundum and transitional alumina grains. They find most of the presolar grains to be corundum. Their dissolution experiments found that, of all phases of alumina that they subjected to acid treatments, only corundum grains survived, while the transitional alumina grains were dissolved. It is therefore possible that transitional alumina presolar grains from AGB stars are present in meteorites, but the acid treatments used to isolate the presolar grains from the rest of the meteorite preferentially destroy any transitional alumina grains present and leave the corundum presolar grains unaffected (Takigawa et al. 2014). They do present infrared absorption spectra of powders of various polymorphs of alumina pressed into KBr pellets. The alpha-alumina infrared spectrum from Takigawa et al. (2014) shows broad features at 13–17 and 20–22 μm very different in appearance from the narrow peaks at 13, 20, and 21 μm from corundum in the models presented here (Figures 1–4). This is consistent with the θ- and δ-alumina curves' broad features spanning ~12–20 μm in the Takigawa et al. (2014) infrared spectra appearing very different from the opacity curves of the samples obtained from heating bayerite at 1273 K and boehmite at 1173 K used in the present study (Figures 1–4). It may be that differences in the opacities used in the present study based on optical properties from Pecharromán et al. (1999) and those presented by Takigawa et al. (2014) are due to differences in the grain shape; a wide range of shapes may be present for the grains of the various polymorphs of alumina whose infrared spectra are presented by Takigawa et al. (2014), while very specific shapes and shape ranges are assumed for this Letter (see Section 3).

An alternative explanation for the 11, 20, 28, and 32 μm features seen in AGB spectra put forth by Guha Niyogi et al. (2011) is that they are due to Fe-rich crystalline silicates. In their study, Guha Niyogi et al. (2011) constructed models using laboratory spectra for Fo9 ($Mg_{0.18}Fe_{1.82}SiO_4$, which is near fayalite in composition) and En1 ($Mg_{0.01}Fe_{0.99}SiO_3$, which is near ferrosilite in composition) along with corundum to match infrared spectra of the AGB star T Cep, one of the stars modeled in the present Letter. By including these Fe-rich silicate components, Guha Niyogi et al. (2011) produced model spectra with peaks near 11, 13, 20, 28, and 32 μm, and, in

addition, produced a "shoulder" at 10 μm like what is seen in the T Cep spectra. Guha Niyogi et al. (2011) did not present T Cep spectra with their models overlaid for direct comparison, as is done in Figures 1–4 of the present study; nevertheless, they did show model and observed spectra on the same plot for comparison, from which some conclusions can be drawn. The peak at 20 μm from the models with crystalline silicates peaks at a longer wavelength than the 20 μm feature in the T Cep spectra. The feature at 28 μm in the T Cep spectra peaks at a longer wavelength than the feature appearing around 27 μm in the crystalline silicate models. The models including components of both Fo9 and En1 also feature a distinct feature at ~18 μm not seen in the T Cep spectrum; also, the ratio of the strength of the 32 μm feature to the strength of the 20 μm feature in the Fo9+En1 models is less than that seen in the T Cep spectra. Though the corundum component included in the present study produces a 21 μm feature that is not seen in observed AGB spectra, the opacities of the materials obtained from heating bayerite at 1273 K and boehmite at 1173 K have the virtue of not producing features not seen in the spectra (e.g., the 18 μm crystalline silicate features) and producing features very close in wavelength to the observed spectra and close in strength ratio (e.g., the 32-to-20 μm feature strength ratio). Guha Niyogi et al. (2011) also noted that Fe-rich silicate grains are not expected to form in stellar outflows, while alumina is expected in AGB star outflows (it is expected to condense in a gas of solar composition; e.g., Grossman 1972).

That the opacities (i.e., total cross-section per mass) of the grains of the samples obtained by heating bayerite at 1273 K and heating boehmite at 1173 K provide good fits of models to data suggests that circumstellar alumina of the same polymorph(s) formed at these temperatures. If the temperature of the formation of the circumstellar alumina polymorph(s) were much higher, the polymorphs would convert to corundum (Pecharromán et al. 1999; Takigawa et al. 2014). Pecharromán et al. (1999) did study samples obtained by heating bayerite and boehmite to other temperatures, but opacities of these other samples did not fit the spectra in the present study as well. As dust tends to be ejected from the star in AGB dust shells, this would suggest that the temperature at the site of formation of these alumina polymorphs is higher than ~1300 K.

Sloan et al. (2003a) noted the correlation between the 13 μm feature and the 20 and 28 μm features. Both the bayerite and boehmite samples from Pecharromán et al. (1999), when heated to increasingly higher temperatures, begin to show signs of a feature forming near 13 microns in their optical properties. Pecharromán et al. (1999) also found increasing α-Al$_2$O$_3$ with increasing temperature. Together, both facts suggest that the 13 μm feature in AGB star spectra may be due in some manner to α-Al$_2$O$_3$, consistent with Glaccum (1999) and DePew et al. (2006).

That Pecharromán et al. (1999) produced their samples by heating aluminum hydroxide compounds bayerite (Al(OH)$_3$) and boehmite (AlOOH) to high temperatures is also very interesting in light of the recent studies at millimeter/submillimeter wavelengths by Kamiński et al. (2016) and Decin et al. (2017). Kamiński et al. (2016) detect emission from AlO, AlOH, AlH, and atomic Al from Mira (Omicron Ceti) using the Atacama Large Millimeter/Submillimeter Array (ALMA), APEX (Güsten et al. 2006), and the *Herschel Space Observatory* (Pilbratt et al. 2010). Decin et al. (2017) find AlO and AlOH emission from the AGB stars R Dor and IK Tau, speculating that clusters of (Al$_2$O$_3$)$_n$ in the gas phase

may be responsible for the 11 μm features in AGB stars (see van Heijnsbergen et al. 2003). Decin et al. (2017) noted that AlO has been found at millimeter wavelengths from the red supergiant star VY CMa by Tenenbaum & Ziurys (2009). Banerjee et al. (2012) found AlO features in near-infrared spectra of various stars, including Miras and OH/IR stars. In addition, De Beck et al. (2017) found AlO in sub-mm/mm observations of Omicron Ceti and R Aqr, and they also found tentative detections of AlO in IK Tau, R Dor, and W Hya. It would be useful to determine if bayerite or boehmite, both of which have compositions (Pecharromán et al. 1999) related to molecules detected around AGB stars, participate in the circumstellar chemistry involving aluminum around evolved stars.

This Letter also highlights the relative lack of laboratory studies of the optical properties of the many polymorphs of alumina besides α-Al$_2$O$_3$ and γ-Al$_2$O$_3$. One starting point would be to explore, in a manner similar to Tamanai et al. (2009), the effects of shape on the opacities of polymorphs of alumina other than the ones that Tamanai et al. (2009) have explored. It would also be useful to explore the formation of alumina by other means in the laboratory; for example, Rietmeijer & Karner (1999) explored gas-phase condensation in a AlO-SiO vapor and found Al$_2$O$_3$ as a product of the condensation. Gobrecht et al. (2016) noted that Al$_2$O$_3$ should form from dimerization of AlO.

ORCID iDs

Benjamin A. Sargent ● https://orcid.org/0000-0001-9855-8261

References

Arenou, F., Luri, X., Babusiaux, C., et al. 2018, arXiv:1804.09375
Banerjee, D. P. K., Varricatt, W. P., Mathew, B., Launila, O., & Ashok, N. M. 2012, ApJL, 753, L20
Begemann, B., Dorschner, J., Henning, T., et al. 1997, ApJ, 476, 199

Bohren, C. F., & Huffman, D. R. 1983, Absorption and Scattering of Light by Small Particles (New York: Wiley)

Day, K. L. 1979, ApJ, 234, 158

De Beck, E., Decin, L., Ramstedt, S., et al. 2017, A&A, 598, A53

Decin, L., Richards, A. M. S., Waters, L. B. F. M., et al. 2017, A&A, 608, A55

DePew, K., Speck, A., & Dijkstra, C. 2006, ApJ, 640, 971

Drimmel, R., Cabrera-Lavers, A., & López-Corredoira, M. 2003, A&A, 409, 205

Eriksson, T. S., Hjortsberg, A., Niklasson, G. A., & Granqvist, C.-G. 1981, ApOpt, 20, 2742

Fabian, D., Henning, T., Jäger, C., et al. 2001, A&A, 378, 228

Fabian, D., Jäger, C., Henning, T., Dorschner, J., & Mutschke, H. 2000, A&A, 364, 282

Gaia Collaboration, Prusti, T., de Bruijne, J. H. J., et al. 2016, A&A, 595, A1

Gaia Collaboration, Brown, A. G. A., Vallenari, A., et al. 2018, arXiv:1804.09365

Glaccum, W. J. 1999, PhD thesis, Univ. Chicago

Gobrecht, D., Cherchneff, I., Sarangi, A., Plane, J. M. C., & Bromley, S. T. 2016, A&A, 585, A6

Grossman, L. 1972, GeCoA, 36, 597

Guha Niyogi, S., Speck, A. K., & Onaka, T. 2011, ApJ, 733, 93

Güsten, R., Nyman, L. Å., Schilke, P., et al. 2006, A&A, 454, L13

Higdon, S. J. U., Devost, D., Higdon, J. L., et al. 2004, PASP, 116, 975

Höfner, S., Bladh, S., Aringer, B., & Ahuja, R. 2016, A&A, 594, A108

Houck, J. R., Roellig, T. L., van Cleve, J., et al. 2004, ApJS, 154, 18

Justtanont, K., Feuchtgruber, H., de Jong, T., et al. 1998, A&A, 330, L17

Kamiński, T., Wong, K. T., Schmidt, M. R., et al. 2016, A&A, 592, A42

Kessler, M. F., Steinz, J. A., Anderegg, M. E., et al. 1996, A&A, 315, L27

Koike, C., Kaito, C., Yamamoto, T., et al. 1995, Icar, 114, 203

Kučinskas, A., Hauschildt, P. H., Brott, I., et al. 2006, A&A, 452, 1021

Kučinskas, A., Hauschildt, P. H., Ludwig, H.-G., et al. 2005, A&A, 442, 281

Lebouteiller, V., Bernard-Salas, J., Sloan, G. C., & Barry, D. J. 2010, PASP, 122, 231

Lebzelter, T., Posch, T., Hinkle, K., Wood, P. R., & Bouwman, J. 2006, ApJL, 653, L145

Leech, K., Kester, D., Shipman, R., et al. 2003, in The ISO Handbook, Vol. V: SWS—The Short Wavelength Spectrometer Version 2.0.1, ESA SP-1262, ed. T. G. Mueller, J. A. D. L. Blommaert, & P. Garcia-Lario (Noordwijk: ESA)

Little-Marenin, I. R., & Price, S. D. 1986, in Summer School on Interstellar Processes: Abstracts of Contributed Papers, NASA Tech. Memorandum 88342, ed. D. J. Hollenbach & H. A. Thronson (Mountain View, CA: NASA Ames Research Center), 137

Luri, X., Brown, A. G. A., Sarro, L. M., et al. 2018, arXiv:1804.09376

Martin, P. G., & Rogers, C. 1987, ApJ, 322, 374

Mathis, J. S. 1990, ARA&A, 28, 37

McClure, M. 2009, ApJL, 693, L81

McDonald, I., Boyer, M. L., van Loon, J. T., et al. 2011b, ApJS, 193, 23

McDonald, I., van Loon, J. T., Sloan, G. C., et al. 2011a, MNRAS, 417, 20

Messenger, S. J., Speck, A., & Volk, K. 2013, ApJ, 764, 142

Min, M., Hovenier, J. W., & de Koter, A. 2003, A&A, 404, 35

Nuth, J. A., Moseley, S. H., Silverberg, R. F., Goebel, J. H., & Moore, W. J. 1985, ApJL, 290, L41

Olofsson, J., Augereau, J.-C., van Dishoeck, E. F., et al. 2009, A&A, 507, 327

Pecharromán, C., Sobrados, I., Iglesias, J. E., González-Carreño, T., & Sanz, J. 1999, JPCB, 103, 6160

Pilbratt, G. L., Riedinger, J. R., Passvogel, T., et al. 2010, A&A, 518, L1

Pitman, K. M., Hofmeister, A. M., Corman, A. B., & Speck, A. K. 2008, A&A, 483, 661

Posch, T., Kerschbaum, F., Mutschke, H., et al. 1999, A&A, 352, 609

Rietmeijer, F. J. M., & Karner, J. M. 1999, JChPh, 110, 4554

Rowan-Robinson, M., & Harris, S. 1983, MNRAS, 202, 797

Sargent, B., Forrest, W. J., D'Alessio, P., et al. 2006, ApJ, 645, 395

Sargent, B. A., Forrest, W. J., Tayrien, C., et al. 2009, ApJ, 690, 1193

Simpson, J. P. 1991, ApJ, 368, 570

Sloan, G. C., Kraemer, K. E., Goebel, J. H., & Price, S. D. 2003a, ApJ, 594, 483

Sloan, G. C., Kraemer, K. E., Price, S. D., & Shipman, R. F. 2003b, ApJS, 147, 379

Sloan, G. C., Levan, P. D., & Little-Marenin, I. R. 1996, ApJ, 463, 310

Sloan, G. C., Matsunaga, N., Matsuura, M., et al. 2010, ApJ, 719, 1274

Smith, V. V., & Lambert, D. L. 1990, ApJS, 72, 387

Smolders, K., Neyskens, P., Blommaert, J. A. D. L., et al. 2012, A&A, 540, A72

Speck, A. K., Barlow, M. J., Sylvester, R. J., & Hofmeister, A. M. 2000, A&AS, 146, 437

Speck, A. K., Corman, A. B., Wakeman, K., Wheeler, C. H., & Thompson, G. 2009, ApJ, 691, 1202

Speck, A. K., Whittington, A. G., & Hofmeister, A. M. 2011, ApJ, 740, 93

Takigawa, A., Tachibana, S., Huss, G. R., et al. 2014, GeCoA, 124, 309

Takigawa, A., Tachibana, S., Nagahara, H., & Ozawa, K. 2015, ApJS, 218, 2

Tamanai, A., Mutschke, H., Blum, J., et al. 2009, A&A, 501, 251

Tenenbaum, E. D., & Ziurys, L. M. 2009, ApJL, 694, L59

Thomas, M. E., Andersson, S. K., Sova, R. M., & Joseph, R. I. 1998, InPhT, 39, 235

Thompson, G. D., Corman, A. B., Speck, A. K., & Dijkstra, C. 2006, ApJ, 652, 1654

Treffers, R., & Cohen, M. 1974, ApJ, 188, 545

van Heijnsbergen, D., Demyk, K., Duncan, M. A., Meijer, G., & von Helden, G. 2003, PCCP, 5, 2515

Wenger, M., Ochsenbein, F., Egret, D., et al. 2000, A&AS, 143, 9

Werner, M. W., Roellig, T. L., Low, F. J., et al. 2004, ApJS, 154, 1

Zeidler, S., Posch, T., & Mutschke, H. 2013, A&A, 553, A81